Assessment of Shortwave Infrared Sea Surface Reflection and Nonlocal Thermodynamic Equilibrium Effects in the Community Radiative Transfer Model Using IASI Data

YONG CHEN

Earth System Science Interdisciplinary Center, University of Maryland, College Park, College Park, Maryland

YONG HAN

Center for Satellite Applications and Research, National Environmental Satellite, Data, and Information Service, College Park, Maryland

PAUL VAN DELST

IMSG Inc., Rockville, and Joint Center for Satellite Data Assimilation, College Park, Maryland

FUZHONG WENG

Center for Satellite Applications and Research, National Environmental Satellite, Data, and Information Service, College Park, Maryland

(Manuscript received 28 November 2012, in final form 20 March 2013)

ABSTRACT

The nadir-viewing satellite radiances at shortwave infrared channels from 3.5 to 4.6 μm are not currently assimilated in operational numerical weather prediction data assimilation systems and are not adequately corrected for applications of temperature retrieval at daytime. For satellite observations over the ocean during the daytime, the radiance in the surface-sensitive shortwave infrared is strongly affected by the reflected solar radiance, which can contribute as much as 20.0 K to the measured brightness temperatures (BT). The nonlocal thermodynamic equilibrium (NLTE) emission in the 4.3-μm CO_2 band can add a further 10 K to the measured BT. In this study, a bidirectional reflectance distribution function (BRDF) is developed for the ocean surface and an NLTE radiance correction scheme is investigated for the hyperspectral sensors. Both effects are implemented in the Community Radiative Transfer Model (CRTM). The biases of CRTM simulations to Infrared Atmospheric Sounding Interferometer (IASI) observations and the standard deviations of the biases are greatly improved during daytime (about a 1.5-K bias for NLTE channels and a 0.3-K bias for surface-sensitive shortwave channels) and are very close to the values obtained during the night. These improved capabilities in CRTM allow for effective uses of satellite data at short infrared wavelengths in data assimilation systems and in atmospheric soundings throughout the day and night.

1. Introduction

The Community Radiative Transfer Model (CRTM) was developed at the Joint Center for Satellite Data Assimilation (JCSDA) (Weng et al. 2005; Han et al. 2006; Chen et al. 2008, 2010, 2012) to simulate the radiances at the top of atmosphere and produce radiance gradients (or Jacobians) for satellite data assimilation and many other remote sensing applications. Since CRTM performs very fast and accurate computations, it has been implemented in the National Centers for Environmental Prediction (NCEP) Global Data Assimilation System, the Global Modeling and Assimilation Office (GMAO) Reanalysis System (Rienecker et al. 2011), and the Microwave Integrated Retrieval System (MIRS) (Boukabara et al. 2011). The CRTM is also supporting the Geostationary Operational Environmental Satellite-R Series (GOES-R) and Joint Polar Satellite System (JPSS) programs for instrument calibration,

Corresponding author address: Yong Chen, NOAA Center for Weather and Climate Prediction, 5830 University Research Court, Station 2878, College Park, MD 20740.
E-mail: yong.chen@noaa.gov

validation, long-term monitoring and trending, and satellite product retrievals.

Today, satellite data assimilation systems and retrieval algorithms are much dependent on the forward models such as CRTM. At the infrared wavelength near $4.3\,\mu m$, CO_2 absorption is strong and the nonlocal thermodynamic equilibrium (NLTE) occurs in the upper atmosphere. If the NLTE process is not taken into account, then the simulated brightness temperatures can include large errors. Also, during daytime, solar radiation near $3.7\,\mu m$ can be reflected by sea surface—a significant error can be introduced if the surface is treated as Lambertian surface, especially when the satellite viewing angle is close to the sun-glint angle. Documents from Monitoring of IR Clear-Sky Radiances over Oceans for Sea Surface Temperature (MICROS; http://www.star.nesdis.noaa.gov/sod/sst/micros/) (Liang et al. 2009), a web-based tool that can be used to validate CRTM performance, indicate that for calculations of solar reflection in the IR shortwave region, a use of the Lambertian assumption can underestimate brightness temperatures (BT) by up to 20 K in the sun-glint area and overestimate by about 2 K in nonsun-glint areas.

At infrared wavelengths, the waves caused by ocean roughness can be simulated through small specular facets whose slopes are distributed according to the Cox and Munk (1954) function. The emission and reflection from each individual facet can be simulated by geometrical optics, and the total emission and reflection from all the facets within a satellite field of view can be statistically derived. Such a physical model is the basis of the parameterized IR sea surface emissivity (IRSSE) model that was implemented in the CRTM (Wu and Smith 1997; Nalli et al. 2008). However, in the earlier version of CRTM version 1.x, the sea surface reflection at the infrared wavelength is treated with a Lambertian type. For reducing this modeling error, the bidirectional reflectance distribution function (BRDF) of Breon (1993) is implemented in the CRTM for calculations of sea surface reflection of solar radiation. The detailed implementation is discussed in section 2. As a result, the CRTM solar reflection model is now consistent with the IRSSE model.

NLTE emission occurs during the daytime in the upper atmosphere (above 40 km), where the rates of creation and annihilation of photons due to solar pumping are greater than the rate of collisions. If the atmosphere is assumed to be in a local thermodynamic equilibrium (LTE), then the local kinetic temperature is defined as the Planck temperature of the radiation field (Kirchhoff 1860). This is invalid in the infrared short wavelength for the upper atmospheres where the NLTE emission occurs in the strong $4.3\text{-}\mu m$ CO_2 absorption band. The effect of NLTE is that the observed satellite radiance is significantly larger than that computed from an LTE approach. DeSouza-Machado et al. (2007) developed a fast NLTE radiative transfer model for the Atmospheric Infrared Sounder (AIRS), which is on board the Earth Observing System (EOS) *Aqua* platform, and they showed that NLTE emission is not important for the $15\text{-}\mu m$ CO_2 band, but that it significantly impacts many channels in the CO_2 $4.3\text{-}\mu m$ band. Several hyperspectral sensors such as the Infrared Atmospheric Sounding Interferometer (IASI) on the *Meteorological Operation-A* (*MetOp-A*) satellite and Cross-Track Infrared Sounder (CrIS) on the *Suomi National Polar-Orbiting Partnership* (*SNPP*) satellite have similar channels in the $4.3\text{-}\mu m$ band but with different spectral resolutions. In this study, we developed a fast NLTE radiative transfer algorithm to model NLTE emission in the $4.3\text{-}\mu m$ spectrum for all three hyperspectral instruments, to allow satellite data assimilation systems and retrieval algorithms to use these channels for upper-tropospheric and stratospheric sounding.

The NLTE effects can be modeled in monochromatic line-by-line (MNLBL) codes such as the General Line-by-Line Atmospheric Transmission and Radiative Transfer Model (GENLN2; Edwards 1992), the Reference Forward Model (RFM) (http://www.atm.ox.ac.uk/RFM), and more recently in the Line-By-Line Radiative Transfer Model (LBLRTM) (Clough et al. 2005). These NLTE models calculate the NLTE modification factors for the optical depth and source function based on the input CO_2 vibrational temperatures profiles (Edwards et al. 1993; López-Puertas and Taylor 2001) and the local kinetic temperatures. These factors can be easily related to the LTE quantities that are usually in the radiative transfer calculations (Edwards et al. 1993, 1998). The channel radiance is then obtained by convolving the monochromatic radiance with the instrument spectral response functions (SRF). Although NLTE effects are modeled in these line-by-line codes, these codes are too computationally intensive for operational use in data assimilation systems and atmospheric retrieval algorithms. In this paper, we use LBLRTM NLTE calculations for a set of reference atmospheric profiles to develop a much faster NLTE model in the CRTM for hyperspectral sensors in operational systems.

Both the BRDF and NLTE models are implemented in CRTM version 2.1, and extensive tests of these two models are conducted in this study. The paper is organized as follows: Section 2 describes the IR sea surface BRDF reflection model. Section 3 details the NLTE fast model developed from LBLRTM. Section 4 presents the assessment of the BRDF and NLTE models with IASI

observations. Finally, section 5 summarizes the conclusions of this study.

2. IR sea surface reflection model

At the height just above the sea surface, the upwelling radiance I is a sum of three terms:

$$I = I_{em} + I_{sky} + I_{sun}, \qquad (1)$$

where the first term is the surface thermal emission, the second is the reflected downwelling thermal sky radiation, and the third is the reflected solar radiation, often called sun glint. The first two terms will not be discussed here, as the thermal emission and the reflected downwelling thermal radiation have been correctly modeled in the CRTM with the IRSSE model.

To derive the sun-glint term, the coordinate system shown in Fig. 1 is adopted. Let $n = \{n_x, n_y, n_z\}$ be an arbitrary unit vector with the components expressed in the Cartesian coordinates. Also, let θ be the polar zenith angle of n (the angle between n and the Z axis) and φ is the azimuth angle of n (the angle between the projection of n in the X–Y plane and the X axis, positive counterclockwise). In Fig. 1, a facet, with the surface normal represented by the unit vector $\mathbf{n}_f$, is located in the center of the coordinate system. The unit vector $\mathbf{n}_r$ points to the direction of the reflected radiation and $\mathbf{n}_s$ to the sun. The angle α between $\mathbf{n}_r$ and $\mathbf{n}_f$ and also between $\mathbf{n}_s$ and $\mathbf{n}_f$ is the specular angle. The angles θ_s, φ_s, θ_r, and φ_r are the zenith and azimuth angles of the sun and the reflected ray, respectively. Let Z be the surface height. The slope of the facet Z_x and Z_y may be written as

$$Z_x = -\frac{\sin(\theta_f)\cos(\varphi_f)}{\cos(\theta_f)} \quad \text{and} \quad Z_y = -\frac{\sin(\theta_f)\sin(\varphi_f)}{\cos(\theta_f)}, \qquad (2)$$

where θ_f and φ_f are the zenith and azimuth angles of the facet normal $\mathbf{n}_f$, respectively. It follows that

$$Z_x^2 + Z_y^2 = \tan^2(\theta_f), \qquad (3)$$

which can be further written as

$$\tan^2(\theta_f) = \frac{n_{f,x}^2 + n_{f,y}^2}{n_{f,z}^2} = \frac{(n_{s,x} + n_{r,x})^2 + (n_{s,y} + n_{r,y})^2}{(n_{s,z} + n_{r,z})^2} = \frac{\sin^2(\theta_s) + \sin^2(\theta_r) + 2\sin(\theta_s)\sin(\theta_r)\cos(\varphi_s - \varphi_r)}{[\cos(\theta_s) + \cos(\theta_r)]^2}. \qquad (4)$$

The slope components Z_x and Z_y can also be expressed in terms of θ_s, φ_s, θ_r, and φ_r, as

$$Z_x = -\frac{n_{s,x} + n_{r,x}}{n_{s,z} + n_{r,z}} = -\frac{\sin(\theta_s)\cos(\varphi_s) + \sin(\theta_r)\cos(\varphi_r)}{\cos(\theta_s) + \cos(\theta_r)},$$

$$Z_y = -\frac{n_{s,y} + n_{r,y}}{n_{s,z} + n_{r,z}} = -\frac{\sin(\theta_s)\sin(\varphi_s) + \sin(\theta_r)\sin(\varphi_r)}{\cos(\theta_s) + \cos(\theta_r)}. \qquad (5)$$

For a large horizontal ocean surface S (such as the footprint of the sensor), the total horizontal surface area of all the facets whose slopes lie in the interval ($Z_x \pm \delta Z_x/2$, $Z_y \pm \delta Z_y/2$) is

$$\delta S' = P(Z_x, Z_y)S\delta Z_x\delta Z_y, \qquad (6)$$

where $P(Z_x, Z_y)$ is the facet slope distribution function. The slope distribution function $P(Z_x, Z_y)$ is given by Cox and Munk (1954),

$$P(Z_x, Z_y) = \frac{1}{\pi\sigma^2}\exp\left(-\frac{Z_x^2 + Z_y^2}{\sigma^2}\right) = \frac{1}{\pi\sigma^2}\exp\left[-\frac{\tan^2(\theta_f)}{\sigma^2}\right], \qquad (7)$$

where σ^2 depends on wind speed W_s (m s^{-1}) as

$$\sigma^2 = 0.003 + 0.005\,12W_s. \qquad (8)$$

The total tilted area is

$$\delta S = \delta S'/\cos(\theta_f) = P(Z_x, Z_y)S\delta Z_x\delta Z_y/\cos(\theta_f). \qquad (9)$$

Let J_s be the radiance of the direct solar radiation at the surface and $\delta\Omega_s$ is the solid angle increment of the radiation. Then, the radiation flux intercepted by the tilted area δS may be expressed as

$$\delta^2 F_s = J_s\delta\Omega_s\cos(\alpha)\delta S, \qquad (10)$$

and the reflected radiation flux, by Fresnel's law, is

$$\delta^2 F_r = \rho(\alpha)\delta^2 F_s = \rho(\alpha)J_s\delta\Omega_s\cos(\alpha)\delta S, \qquad (11)$$

where $\rho(\alpha)$ is the Fresnel reflectance [Nalli et al. 2008, their Eq. (5)]. The Fresnel reflectance is a function of the complex index of refraction and the specular angle α
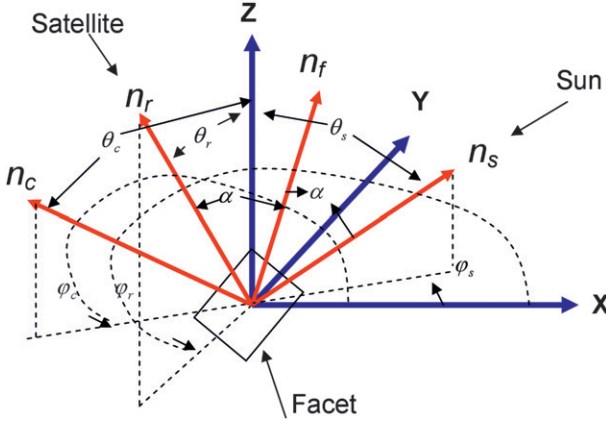
FIG. 1. Coordinate system for facet reflection. Facet is located at the origin with surface normal $\mathbf{n}_f$. Unit vector $\mathbf{n}_r$ points to the direction of the reflected radiation (or to the direction of observer), $\mathbf{n}_c$ to the specular reflection direction on a calm surface, and $\mathbf{n}_s$ to the sun. Angle α between $\mathbf{n}_r$ and $\mathbf{n}_f$ and also between $\mathbf{n}_s$ and $\mathbf{n}_f$ is the specular angle. Angles θ_s, φ_s, θ_c, φ_c, θ_r, and φ_r are the zenith and azimuth angles of the sun, of the reflected ray at the calm surface, and of the reflected ray at the facet surface, respectively.

with respect to the local normal. The cosine of the specular angle α in Eq. (11) can be derived as

$$
\begin{aligned}
\cos^2(\alpha) &= (\mathbf{n}_f \cdot \mathbf{n}_r)^2 = (1 + \mathbf{n}_s \cdot \mathbf{n}_r)/2 \\
&= (1 + n_{s,x}n_{r,x} + n_{s,y}n_{r,y} + n_{s,z}n_{r,z})/2 \\
&= \frac{1 + \sin(\theta_s)\sin(\theta_r)\cos(\varphi_s - \varphi_r) + \cos(\theta_s)\cos(\theta_r)}{2}.
\end{aligned}
\tag{12}
$$

The sensor measures the reflected radiance from the surface S. Let δI_r be the increment of the reflected radiance, which is related to the reflected radiation flux $\delta^2 F_r$ in Eq. (11),

$$
\delta I_r = \frac{\delta^2 F_r}{S \cdot \cos(\theta_r)\delta\Omega_r},
\tag{13}
$$

where $\delta\Omega_r$ is the increment of the solid angle of the reflected radiation. The increment $\delta\Omega_r$ is the result of the increment $\delta Z_x \delta Z_y$, as the two slope components Z_x and Z_y of the facet vary within ($Z_x \pm \delta Z_x/2$, $Z_y \pm \delta Z_y/2$), the facet surface normal $\mathbf{n}_f$ varying within a solid angle $\delta\Omega_f$ and the direction of the reflected ray varying in the solid angle $\delta\Omega_r$. Mathematically, the relationships among $\delta Z_x \delta Z_y$, $\delta\Omega_f$, and $\delta\Omega_r$ can be derived using the equation

$$
\delta Z_x \delta Z_y = \begin{vmatrix} \dfrac{\partial Z_x}{\partial \theta} & \dfrac{\partial Z_x}{\partial \varphi} \\[2mm] \dfrac{\partial Z_y}{\partial \theta} & \dfrac{\partial Z_y}{\partial \varphi} \end{vmatrix} \delta\theta\,\delta\varphi,
\tag{14}
$$

where the quantity before $\delta\theta\delta\varphi$ on the right-hand side of the equation is the Jacobian. Taking the Jacobians of Eqs. (2) and (5), and noting that $\sin(\theta)\delta\theta\delta\varphi = \delta\Omega$ and θ_s and φ_s are constant in the Jacobian evaluations, the following can be obtained:

$$
\delta Z_x \delta Z_y = \frac{\delta\Omega_f}{\cos^3(\theta_f)} = \frac{\delta\Omega_r}{4\cos^3(\theta_f)\cos(\alpha)}.
\tag{15}
$$

To derive Eq. (15), both Eqs. (4) and (12) are used.

Since the incident flux on a unit horizontal surface within the solid angle $\delta\Omega_s$ is

$$
\delta F_i = J_s \delta\Omega_s \cos(\theta_s),
\tag{16}
$$

the BRDF of the rough sea surface, according to the definition, can be written by using Eqs. (9), (11), (13), (15), and (16), as [Breon 1993, Eq. (A8)]

$$
\mathrm{BRDF}(\theta_s, \varphi_s, \theta_r, \varphi_r) = \frac{\delta I_r}{\delta F_i} = \frac{\rho(\alpha)P(Z_x, Z_y)}{4\cos(\theta_s)\cos(\theta_r)\cos^4(\theta_f)}.
\tag{17}
$$

With the BRDF, the reflected radiance in Eq. (1) can be computed as

$$
\begin{aligned}
I_{\mathrm{sun}} &= \int_{\Omega_s} J_s \cos(\theta_s)\mathrm{BRDF}(\theta_s, \varphi_s, \theta_r, \varphi_r)\, d\Omega_s \\
&\approx J_s \cos(\theta_s)\mathrm{BRDF}(\theta_s, \varphi_s, \theta_r, \varphi_r)\Omega_s \\
&= E_s \cos(\theta_s)\mathrm{BRDF}(\theta_s, \varphi_s, \theta_r, \varphi_r),
\end{aligned}
\tag{18}
$$

where Ω_s is the solid angle of the solar disk seen from the surface and E_s is the irradiance of the sun at the surface.

The so-called sun-glint angle is defined as the angle between $\mathbf{n}_o$ (the direction of the satellite observation, or the direction of reflected radiation $\mathbf{n}_r$) and the specular reflection direction $\mathbf{n}_c$ on a calm surface (horizontal surface). The glint angle θ_g is obtained as

$$
\begin{aligned}
\cos(\theta_g) &= \mathbf{n}_o \cdot \mathbf{n}_c = (2\mathbf{n}_s \cdot \mathbf{n}_z)\mathbf{n}_z \cdot \mathbf{n}_o - \mathbf{n}_s \cdot \mathbf{n}_o \\
&= \cos(\theta_s)\cos(\theta_o) - \sin(\theta_s)\sin(\theta_o)\cos(\varphi_s - \varphi_o).
\end{aligned}
\tag{19}
$$

3. Fast NLTE radiative transfer model

A special version of LBLRTM version 11.7 for NLTE (a couple of minor NLTE bug fixes are included) was used to compute daytime radiances from the University of Maryland, Baltimore County (UMBC) set of 48 diverse training profiles (Strow et al. 2003), as a function of 13 sensor zenith angles and six solar zenith angles to generate regression data for the parameterized fast NLTE RT model for hyperspectral sensors such as AIRS, IASI, and CrIS. The LBLRTM used for this work applies the same vibrational temperature profile to all lines for a given state, ignoring the isotopologue number of the line, which may introduce a possible error of up to 0.2 K (V. H. Payne 2010, personal communication). The CRTM basically is a LTE model, and its transmittance coefficients are based on regression algorithms (Chen et al. 2010, 2012) to relate the convolved channel transmittance with the atmospheric-state variables. The channel radiance can then be obtained by using an efficient radiative transfer solver (Liu and Weng 2006). To take account of the NLTE effect in the CRTM more efficiently, a simple additive correction to the LTE radiance is applied. For each channel, the NLTE radiance can be related to LTE radiance,

$$R_{ch}^{NLTE} = R_{ch}^{LTE} + \Delta R_{ch}, \qquad (20)$$

where R_{ch}^{NLTE} and R_{ch}^{LTE} are the convolved channel radiance, either through direct convolution from SRF (for AIRS) or through Fourier transform by converting radiances to interferograms, applying the sensor apodization function, and then inverse Fourier transforming back to channel radiance (for IASI and CrIS). For each sensor zenith angle and solar zenith angle pair, the channel radiance difference ΔR_{ch} can be estimated by using three predictors:

$$\Delta R_{ch}(\theta_i, \vartheta_j) = c_0(\theta_i, \vartheta_j) + c_1(\theta_i, \vartheta_j) T_{m1} + c_2(\theta_i, \vartheta_j) T_{m2}, \qquad (21)$$

where c_i (i = 0, 1, 2) are the regression coefficients, T_{m1} is the mean kinetic temperature from 0.005 to 0.2 hPa, and T_{m2} is the mean kinetic temperature from 0.2 to 52 hPa. In Eq. (21) $\theta_i, i = 1, 2, \ldots, 13$, is the sensor zenith angle at the surface of the earth, corresponding to the airmass range from 1.0 to 4.0 with an even interval of 0.25, and $\vartheta_j, j = 1, 2, \ldots, 6$, is the solar zenith angle (0°, 40°, 60°, 80°, 85° and 90°). Figure 2 shows that the fitting errors for the fast model using Eq. (21) and LBLRTM calculations using Eq. (20) were very small, with mean differences on the order of 0.002 K and an RMS difference on the order of 0.05 K for the AIRS, CrIS, and IASI
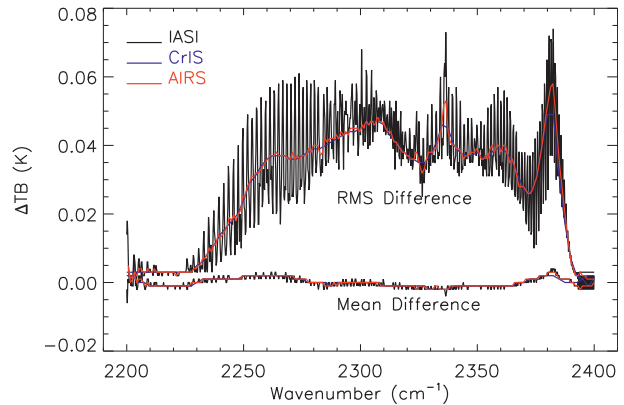

FIG. 2. Fitting errors of the fast NLTE model compared to LBLRTM, with a mean difference on the order of 0.002 K and an RMS difference on the order of 0.05 K for all the hyperspectral sensors AIRS, CrIS, and IASI.

sensors. For any user input sensor zenith angle and solar zenith angle within the training limitation (sensor zenith angle less than 75.5225°, and solar zenith angle less than 90°), the radiance difference can be calculated by interpolating from Eq. (20):

$$\Delta R_{ch}(\theta, \vartheta) = \sum_{i=1}^{2} \sum_{j=1}^{2} w_{i,j}(\theta, \vartheta) \Delta R_{ch}(\theta_i, \vartheta_j), \qquad (22)$$

where $w_{i,j}(\theta, \vartheta)$ are the interpolation weights. The weights at the user input sensor zenith angle and solar zenith angle are obtained through bilinear interpolation from the four secants of the angle (two sensor angles and two solar angles) that bracket the desired value. The NLTE channel radiance can be easily and quickly computed in the CRTM via Eq. (20).

4. Comparison between simulations and IASI observation data

In this study, we use IASI instead of AIRS or CrIS data to test the accuracy of the sea surface reflection model and the NLTE fast model in CRTM, since IASI has the highest spectral resolution (with a channel interval of 0.25 cm^{-1}) and covers all of the shortwave IR spectrum from 2000.0 to 2760.0 cm^{-1}. Four representative days of IASI observations (25 May 2011, 25 August 2011, 25 November 2011, and 25 February 2012), whose radiances passed a strict spatial uniformity test and a cloud test over ocean [using collocated Advanced Very High Resolution Radiometer (AVHRR) to detect cloud contamination of IASI data], were selected. The effects of possible contamination by clouds or spatially varying humidity in the IASI observations were further reduced
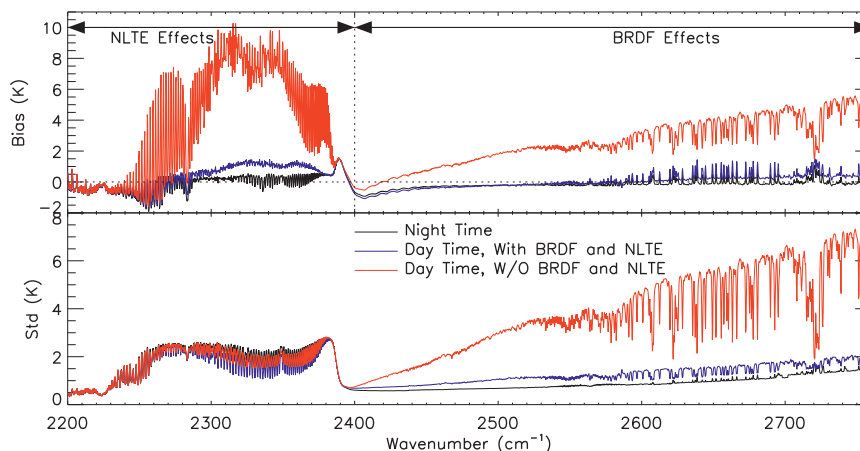
FIG. 3. (top) BT(observation) minus BT(simulation) biases and (bottom) standard deviations between IASI observations and CRTM simulations. Red curves show the daytime results when the BRDF and NLTE models were turned off. Blue curves show daytime results when the BRDF and NLTE models were turned on. Black curves show nighttime results.

by using the European Centre for Medium-Range Weather Forecasts (ECMWF) hyperspectral IR cloud detection algorithm (McNally and Watts 2003) to select clear channels. The water vapor, ozone, and temperature profiles are from the ECMWF analysis model fields, and the CO_2 mixing ratio profile is from the averaged CRTM training profile set. Daytime and nighttime data are separated. The total number of clear data points from the four days is about 150 000 for both daytime and nighttime. Comparisons were made by running the CRTM version 2.1 with both the NLTE and BRDF models turned on and turned off.

Figure 3 summarizes the brightness temperature biases and standard deviations between IASI observations and CRTM simulations between 2200 and 2760 cm^{-1} for the four days. The biases using the NLTE model during the daytime are dramatically reduced compared to the LTE results from 2200 to 2400 cm^{-1}. The daytime NLTE biases for all the NLTE-affected channels are less than 1.5 K, compared to a daytime LTE model that would have biases larger than 8 K. The CRTM NLTE model underestimates the NLTE effect by up to 1.0–1.5 K, which is consistent with a previous study using the AIRS NLTE model (DeSouza-Machado et al. 2007). The CRTM NLTE model and the AIRS NLTE model use different baseline MNLBL models [LBLRTM versus kCompressed Radiative Transfer Algorithm (kCARTA)] for training, and different parameterization schemes. However, both fast models used the same UMBC 48 training profiles and six solar zenith angles, modeled NLTE as an additive correction to LTE radiances, and applied the same vibrational temperature profile in the baseline MNLBL models. The remaining approximately

1.0–1.5-K bias at the NLTE channels may come from the error sources common to both of the fast models. Further investigation is needed to understand the sources of the bias. The biases using the BRDF model are reduced significantly (~0.3 K) compared to Lambertian surface reflection (~3–5 K) at the surface-sensitive shortwave channels between 2500 and 2760 cm^{-1} during daytime. The daytime biases from the BRDF model are slightly larger than nighttime biases, but the differences are within ~0.5 K for all the surface-sensitive shortwave channels.

Figure 4 shows the daytime BT biases in the shortwave IR channels between IASI observations and CRTM simulations with the NLTE and BRDF models turned off (LTE model and Lambertian reflection) as a function of solar zenith angle (top panel) and as a function of sun-glint angle (bottom panel). The biases in the CO_2 NLTE channels from 2260 to 2380 cm^{-1}, which have weighting functions that peak high in the atmosphere, can be as large as 10 K, whereas the biases for the rest of the NLTE channels that have weighting functions peaking lower in the atmosphere are less than 1 K. These biases are very consistent regardless of the solar zenith angle and sun-glint angle. However, the biases in the surface-sensitive shortwave channels show very strong dependence on solar zenith angle and sun-glint angle. It can be seen that near the sun-glint angle (less than 30°), the Lambertian reflection assumption in the CRTM underestimates the radiance by more than 20 K, and in the off-sun-glint area the impact is very small, only ~1 K. The biases as a function of the solar zenith angle and as a function of sun-glint angle show very high correlation. When the solar zenith angle is smaller, the reflected solar
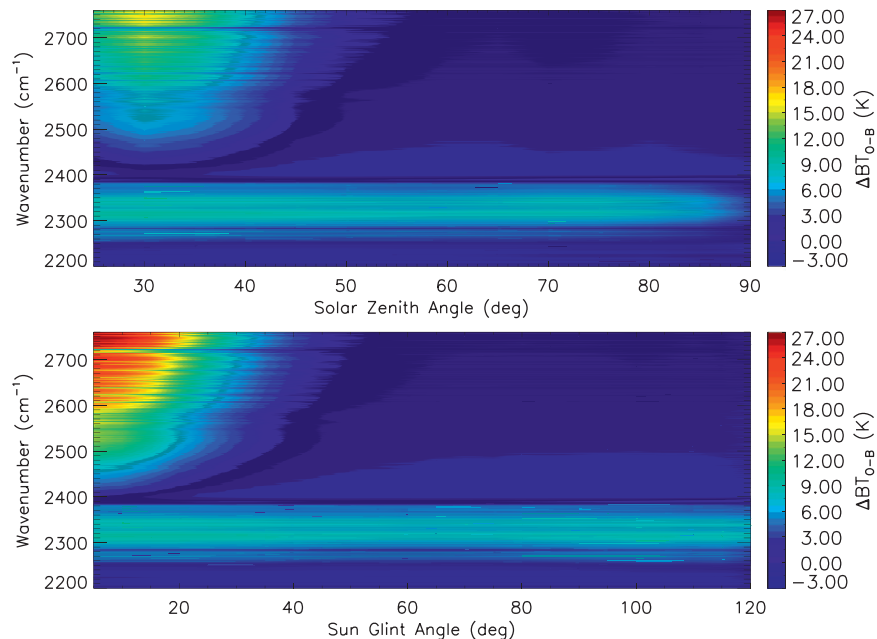
FIG. 4. Daytime biases in the shortwave IR channels between IASI observations and CRTM simulations with the BRDF and NLTE models turned off. (top) Biases as a function of solar zenith angle (horizontal axis, °) and IASI channel in wavenumber (vertical axis, cm^{-1}). (bottom) Biases as a function of sun-glint angle and IASI channel (cm^{-1}).

radiation becomes larger [from Eq. (18)]. The same is true for the sun-glint angle: when the angle is smaller, most of the solar energy will be reflected off the surface of the ocean to reach the IASI sensor, causing larger brightness temperatures. Without considering the BRDF reflection at the sun-glint angle, the biases would be significant.

Figure 5 shows the daytime biases as a function of solar zenith angle and as a function of sun-glint angle in the shortwave IR channels between the same IASI observations as in Fig. 4 and CRTM simulations but now *using* the BRDF and NLTE models. Compared to Fig. 4, it is clearly evident that the NLTE model has significantly reduced the biases for the 4.3-μm CO_2 channels to ~1.0 K, independent of the solar zenith angle below ~70°. Beyond this angle, the biases then decrease for large solar zenith angles. The biases for these CO_2 channels are independent of sun-glint angle because of the strong CO_2 absorption; these spectral radiances can hardly reach the surface and the reflection is even less likely to reach to the top of atmosphere. The consistent biases for the NLTE channels can be empirically corrected by introducing a channel-dependent adjustment factor to the radiance difference between the NLTE and LTE model (DeSouza-Machado et al. 2007). Comparisons between Figs. 4 and 5 indicate that the BRDF model significantly improved the surface-sensitive

shortwave channels' biases over the Lambertian reflection assumption during the daytime over the ocean surface. When the sun-glint angle is greater than 30°, the biases are reduced to less than 1 K. However, negative biases up to 2–3 K still exist for small sun-glint angles. These errors are significant in some applications, such as sea surface temperature retrievals. Future work is needed to analyze the causes and to develop methods to reduce the errors.

5. Conclusions

We have demonstrated a BRDF reflection model and a fast model of NLTE effects in the CRTM for the temperature sounding 4.3-μm CO_2 band and shortwave IR window channels for hyperspectral IR sensors. The accuracy of these models is sufficient to make the daytime radiance simulation very close to the nighttime simulation. The NLTE channels' biases are reduced to less than 1.5 K, and the shortwave IR window channels' biases are around 0.3 K. The daytime biases from the BRDF model are slightly larger than nighttime biases, but the differences are within ~0.5 K for all surface-sensitive shortwave channels. The addition of channels sensitive to the surface and to NLTE allows data assimilation systems and retrievals algorithms to cover both the lower-air and upper-air atmosphere at both day
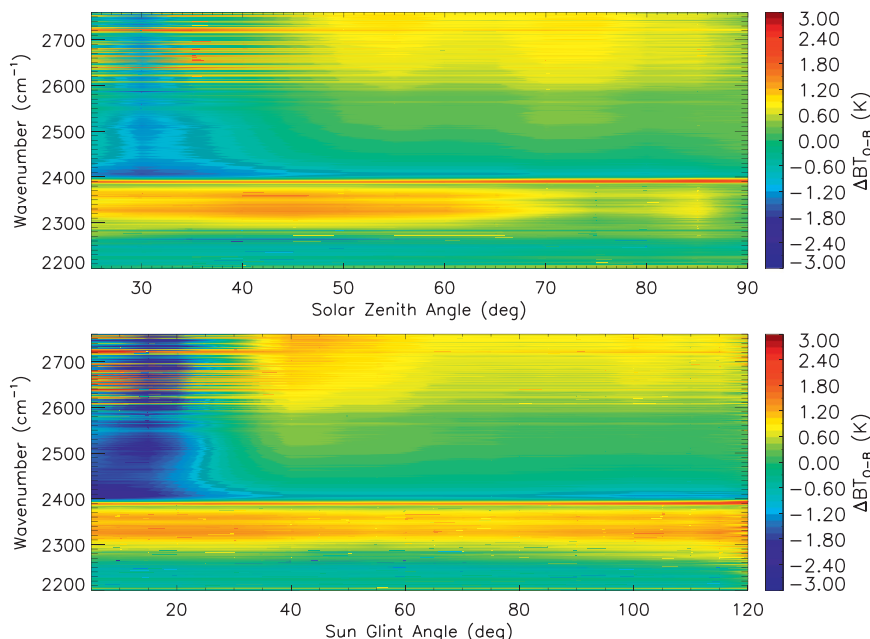
FIG. 5. As in Fig. 4, but the BRDF and NLTE models in CRTM were turned on. Temperature color bar scale (from −3 to 3 K) is much smaller than that from Fig. 4 (from −3 to 27 K).

and night. Future improvements for the BRDF and NLTE models may include reducing the slightly larger negative bias at the lower sun-glint angles for the surface-sensitive shortwave channels and resolving the consistent positive bias across the 4.3-μm CO_2 band.

REFERENCES

Boukabara, S.-A., and Coauthors, 2011: MiRS: An all-weather 1DVAR satellite data assimilation and retrieval system. *IEEE Trans. Geosci. Remote Sens.,* **49,** 3249–3272, doi:10.1109/TGRS.2011.2158438.

Breon, F. M., 1993: An analytical model for the cloud-free atmosphere/ocean system reflectance. *Remote Sens. Environ.,* **43,** 179–192.

Chen, Y., F. Weng, Y. Han, and Q. Liu, 2008: Validation of the Community Radiative Transfer Model (CRTM) by using CloudSat data. *J. Geophys. Res.,* **113,** D00A03, doi:10.1029/2007JD009561.

——, Y. Han, P. Van Delst, and F. Weng, 2010: On water vapor Jacobian in fast radiative transfer model. *J. Geophys. Res.,* **115,** D12303, doi:10.1029/2009JD013379.

——, ——, and F. Weng, 2012: Comparison of two transmittance algorithms in the Community Radiative Transfer Model: Application to AVHRR. *J. Geophys. Res.,* **117,** D06206, doi:10.1029/2011JD016656.

Clough, S. A., M. W. Shephard, E. J. Mlawer, J. S. Delamere, M. J. Iacono, K. Cady-Pereira, S. Boukabara, and P. D. Brown, 2005: Atmospheric radiative transfer modeling: A summary of the AER codes. *J. Quant. Spectrosc. Radiat. Transfer,* **91,** 233–244.

Cox, C., and W. Munk, 1954: Measurements of the roughness of the sea surface from photographs of the sun's glitter. *J. Opt. Soc. Amer.,* **44,** 838–850.

DeSouza-Machado, S. G., L. L. Strow, S. E. Hannon, H. E. Motteler, M. López-Puertas, B. Funke, and D. P. Edwards, 2007: Fast forward radiative transfer modeling of 4.3 μm nonlocal thermodynamic equilibrium effects for infrared temperature sounders. *Geophys. Res. Lett.,* **34,** L01802, doi:10.1029/2006GL026684.

Edwards, D. P., 1992: GENLN2: A General Line-by-Line Atmospheric Transmittance and Radiance Model; version 3.0 description and users guide. NCAR Tech. Note NCAR/TN-367+STR, 147 pp.

——, M. López-Puertas, and M. López-Valverde, 1993: Nonlocal thermodynamic equilibrium studies studies of 15-μm bands of CO_2 for atmospheric remote sensing. *J. Geophys. Res.,* **98,** 14 955–14 977.

——, ——, and R. R. Gamache, 1998: The non-LTE correction to the vibrational component of the internal partition sum for atmospheric calculations. *J. Quant. Spectrosc. Radiat. Transfer,* **59,** 423–436.

Han, Y., P. van Delst, Q. Liu, F. Weng, B. Yan, R. Treadon, and J. Derber, 2006: JCSDA Community Radiative Transfer

Model (CRTM)—Version 1. NOAA Tech. Rep. NESDIS 122, 40 pp.

Kirchhoff, G., 1860: Über das Verhältniss zwischen dem Emissionsvermögen und dem Absorptionsvermögen der Körper für Wärme and Licht. *Ann. Phys. Chem.,* **109,** 275–301.

Liang, X.-M., A. Ignatov, and Y. Kihai, 2009: Implementation of the Community Radiative Transfer Model in Advanced AVHRR Clear-Sky Processor for Oceans and validation against nighttime AVHRR radiances. *J. Geophys. Res.,* **114,** D06112, doi:10.1029/2008JD010960.

Liu, Q., and F. Weng, 2006: Advanced doubling-adding method for radiative transfer in planetary atmospheres. *J. Atmos. Sci.,* **63,** 3459–3465.

López-Puertas, M., and F. W. Taylor, 2001: *Non-LTE Radiative Transfer in the Atmosphere.* Series on Atmospheric, Oceanic, and Planetary Physics, Vol. 3, World Scientific, 487 pp.

McNally, A. P., and P. D. Watts, 2003: A cloud detection algorithm for high-spectral-resolution infrared sounders. *Quart. J. Roy. Meteor. Soc.,* **129,** 3411–3423.

Nalli, N. R., P. J. Minnett, and P. van Delst, 2008: Emissivity and reflection model for calculating unpolarized isotropic water suface-leaving radiance in the infrared. I: Theoretical development and calculations. *Appl. Opt.,* **47,** 3701–3721.

Rienecker, M. M., and Coauthors, 2011: MERRA: NASA's Modern-Era Retrospective Analysis for Research and Applications. *J. Climate,* **24,** 3624–3648.

Strow, L. L., S. E. Hannon, S. D. Souza-Machado, H. E. Mottler, and D. Tobin, 2003: An overview of the AIRS radiative transfer model. *IEEE Trans. Geosci. Remote Sens.,* **41,** 303–313.

Weng, F., Y. Han, P. van Delst, Q. Liu, and B. Yan, 2005: JCSDA community radiative transfer model (CRTM). *Proc. 14th Int. ATOVS Study Conf.,* Beijing, China, International TOVS Working Group, 217–222.

Wu, X., and W. L. Smith, 1997: Emissivity of rough sea surface for 8–13 μm: Modeling and verification. *Appl. Opt.,* **36,** 2609–2619.